

Contents lists available at ScienceDirect

# Journal of Computational and Applied Mathematics

journal homepage: www.elsevier.com/locate/cam



# A novel Large Eddy Simulation model for the Quasi-Geostrophic equations in a Finite Volume setting



Michele Girfoglio a,\*, Annalisa Quaini b, Gianluigi Rozza a

- <sup>a</sup> SISSA, International School for Advanced Studies, Mathematics Area, mathLab, via Bonomea, Trieste 265 34136, Italy
- <sup>b</sup> Department of Mathematics, University of Houston, Houston TX 77204, USA

#### ARTICLE INFO

Article history: Received 31 January 2022 Received in revised form 15 July 2022

Keywords: Finite Volume approximation Large Eddy Simulation BV-α model Quasi-Geostrophic equations Nonlinear filter stabilization

#### ABSTRACT

We present a Large Eddy Simulation (LES) approach based on a nonlinear differential low-pass filter for the simulation of two-dimensional barotropic flows with under-refined meshes. For the implementation of such model, we choose a segregated three-step algorithm combined with a computationally efficient Finite Volume method. We assess the performance of our approach with the classical double-gyre wind forcing benchmark. The numerical experiments we present demonstrate that our nonlinear filter is an improvement over a linear filter since it is able to recover the four-gyre pattern of the time-averaged stream function even with extremely coarse meshes. In addition, our LES approach provides an average kinetic energy that compares well with the one computed with a Direct Numerical Simulation.

© 2022 Elsevier B.V. All rights reserved.

#### 1. Introduction

Accurate numerical simulations of geophysical flows are not only an essential tool for ocean and weather forecast, but they could also provide insights on the mechanisms governing climate change. In such simulations, two-dimensional turbulence represents a major challenge. While in the Kolmogorov three-dimensional turbulence theory [1,2] the kinetic energy is transferred from the large scales to the small scales, in the Kraichnan–Batchelor–Leith two-dimensional turbulence theory [3–5] average inverse (i.e., from small to large scales) energy and direct (from large to small scales) enstrophy cascades are observed.

One of the simplest models for geophysical flow is given by the Quasi-Geostrophic equations (QGE): see, e.g., [6–8] for mathematical and physical fundamentals, [9–11] for some advanced applications and [12] for a recent review on this model. Despite the simplification in the QGE, when the Munk scale (a length that depends on two nondimensional quantities, the Rossby number and the Reynolds number) is small the numerical simulation of the QGE becomes computationally challenging since very fine meshes are required. In addition, often long time intervals have to be simulated, making the computational cost prohibitive. A way to reduce the computational cost is to adopt a Large Eddy Simulation (LES) approach that allows to use a coarser mesh by modeling the effect of the small scales that do not get resolved.

In this paper, we focus on a LES model called BV- $\alpha$  [13–16] that introduces a filter for the nonlinear term of the QGE model in order to correctly simulate physical flow when the mesh size is greater than Munk scale. Two are the main novelties of our work: (i) the use of a nonlinear indicator function to identify the regions of the domain where the flow

E-mail addresses: mgirfogl@sissa.it (M. Girfoglio), quaini@math.uh.edu (A. Quaini), grozza@sissa.it (G. Rozza).

<sup>\*</sup> Corresponding author.

needs regularization and (ii) the space discretization with a computationally efficient Finite Volume method. Nonlinear filter stabilization has been adopted successfully for simulating two and three-dimensional incompressible flows; see, e.g., [17-20]. However, to the best of our knowledge, it is the first time that such a methodology is utilized for geophysical flows. The advantage of a Finite Volume method lies in preserving conservative quantities for the governing equations. For this reason, Finite Volume approximations have been widely used for LES models of incompressible flows. Other authors have chosen to discretize the linear BV- $\alpha$  model with a Finite Difference method [13,14] or a Finite Element method [15,16].

In order to assess the performance of the proposed LES approach, we consider the classical double-gyre wind forcing benchmark [13-16,21,22]. We present numerical results for test cases: (i) Rossby number 0.0036, Reynolds number 450 and (ii) Rossby number 0.008, Reynolds number Re = 1000. Most of the works on the double-gyre wind forcing benchmark consider Rossby number 0.0016 and Reynolds number 200 [13-16], while flows at Rossby number 0.0036, Reynolds number 450 are studied in [9,22]. Our test case (ii) features higher Rossby and Reynolds numbers than what studied in the literature and is therefore more challenging.

The paper is organized as follows. In Section 2, we introduce the QGE and the BV- $\alpha$  models and the associated strategy for time and space discretization. Numerical results are reported in Section 3, while conclusions and future perspectives are presented in Section 4.

## 2. Problem definition

# 2.1. Quasi-geostrophic equations

We consider the motion of a two-dimensional rotating homogeneous flow in a two-dimensional fixed domain  $\Omega$  over a time interval of interest  $(t_0, T)$ . We assume that such flow can be modeled by the quasi-geostrophic equations (QGE) in stream function-potential vorticity formulation, also known as the barotropic vorticity equation (BVE). In order to state the BVE, let  $\hat{q} = \hat{\omega} + \beta \hat{y}$  be the dimensional potential vorticity, where  $\hat{\omega}$  is the dimensional vorticity,  $\hat{y}$  is the dimensional vertical coordinate, and  $\beta$  is the gradient of the Coriolis parameter at the basin center. For convenience, we switch to non-dimensional variables by introducing a characteristic length L and a characteristic velocity U. The non-dimensional potential vorticity q is defined as:

$$q = Ro \omega + y, \quad Ro = \frac{U}{\beta L^2}$$
 (1)

where  $\omega$  is the non-dimensional vorticity, y is the non-dimensional vertical coordinate, and Ro is the Rossby number, which is the ratio of inertial force to Coriolis force. The BVE in non-dimensional variables reads:

$$\partial_t q + \nabla \cdot ((\nabla \times \psi) \, q) - \frac{1}{R_{\mathbf{P}}} \Delta q = F \quad \text{in } \Omega \times (t_0, T), \tag{2}$$

where  $\partial_t$  denotes the time derivative, Re is the Reynolds number (i.e., the ratio of inertial force to viscous force), F denotes an external forcing, and  $\psi = (0, 0, \psi)$  with  $\psi$  being the stream function. The kinematic relationship between vorticity  $\omega$  and the stream function  $\psi$  yields the following Poisson equation

$$\omega = -\Delta \psi \quad \text{in } \Omega \times (t_0, T). \tag{3}$$

Using (1), Eq. (3) can be rewritten in terms of q:

$$q = -\operatorname{Ro}\Delta\psi + y \quad \text{in } \Omega \times (t_0, T). \tag{4}$$

To close problem (2), (4), proper boundary conditions and initial data should be provided. Following [9,13–16], we enforce  $\psi = \omega = 0$  on  $\partial \Omega$  and set the initial condition  $\omega(x, y, t_0) = 0$  in  $\Omega$ , which in terms of  $\psi$  and q become

$$\psi = 0 \quad \text{on } \partial\Omega \times (t_0, T), \tag{5}$$

$$q = y \quad \text{on } \partial\Omega \times (t_0, T),$$
 (6)

$$q(x, y, t_0) = y \quad \text{in } \Omega. \tag{7}$$

Summarizing, the barotropic vorticity problem is given by Eqs. (2), (4) endowed with boundary conditions (5)–(6) and initial data (7).

# 2.2. The BV- $\alpha$ problem

Despite the fact that the QGE model is a toy problem describing the main features of geophysical flows under certain simplifying assumptions, its Direct Numerical Simulation (DNS) is still hindered by a prohibitive computational cost. This is especially true in the case of climate simulations that require long time intervals (of the order of centuries). A DNS for the QGE model requires a mesh with mesh size smaller than the Munk scale:

$$\delta_{\rm M} = L \sqrt[3]{\frac{\rm Ro}{\rm Re}}.$$
 (8)

Notice that larger Reynolds numbers and smaller Rossby numbers lead to a small Munk scale and thus the need for fine meshes. When the mesh size fails to resolve the Munk scale, the simulation provides a non-physical solution. A possible remedy is to introduce a model for the small (unresolved) scales in order to recover the physical solution while resolving only the large spatial scales and so containing the computational cost.

In this paper, we propose a nonlinear variant of the so-called  $BV-\alpha$  model [13–16] that couples the BVE model with a differential filter. Such model reads:

$$\partial_t q + \nabla \cdot ((\nabla \times \psi) \, q) - \frac{1}{\mathsf{Re}} \Delta q = F \quad \text{in } \Omega \times (t_0, T), \tag{9}$$

$$-\alpha^2 \nabla \cdot (a(q) \nabla \overline{q}) + \overline{q} = q \quad \text{in } \Omega \times (t_0, T), \tag{10}$$

$$-\operatorname{Ro}\Delta\psi + y = \overline{q} \quad \text{in } \Omega \times (t_0, T), \tag{11}$$

where  $\bar{q}$  is the filtered vorticity,  $\alpha$  can be interpreted as the filtering radius and  $a(\cdot)$  is a scalar function such that:

 $a(a) \simeq 0$  where the flow field does not need regularization:

 $a(q) \simeq 1$  where the flow field does need regularization.

By setting  $a(q) \equiv 1$  in (9)–(11) we retrieve the classical BV- $\alpha$  model [13–16]. This model has the advantage of making the operator in the filter equations linear and constant in time, but we will show that its effectivity is rather limited when very coarse meshes are considered.

Function a is called indicator function and it plays a key role in the success of the differential filter. Taking inspiration from the large body of work on the Leray- $\alpha$  model [17,23-26], we propose the following indicator function:

$$a(q) = \frac{|\nabla q|}{\max\left(1, \|\nabla q\|_{\infty}\right)}.$$
(12)

Function (12) is mathematically convenient because of its strong monotonicity properties.

We will refer to Eq. (9)–(11) with indicator function given by (12) as the nonlinear BV- $\alpha$  (or BV- $\alpha$ -NL) model.

#### 2.3. Time and space discretization

Let us start with the time discretization of problem (9)-(11). Let  $\Delta t \in \mathbb{R}$ ,  $t^n = t_0 + n\Delta t$ , with  $n = 0, \ldots, N_T$  and  $T = t_0 + N_T \Delta t$ . We denote by  $f^n$  the approximation of a generic quantity f at the time  $t^n$ . For simplicity, we present the discrete scheme using the Backward Differentiation Formula of order 1 (BDF1) to discretize the time derivative in (9). However, in Section 3.1 we will report results obtained with both BDF1 and BDF2. The time-discrete scheme reads as follows: given  $q^0$ , for  $n \ge 0$  find the solution  $(q^{n+1}, \psi^{n+1}, \overline{q}^{n+1})$  of system:

$$\frac{1}{\Delta t}q^{n+1} + \nabla \cdot \left( \left( \nabla \times \psi^{n+1} \right) q^{n+1} \right) - \frac{1}{Re} \Delta q^{n+1} = b^{n+1}, \tag{13}$$

$$-\alpha^2 \nabla \cdot \left(a^{n+1} \nabla \overline{q}^{n+1}\right) + \overline{q}^{n+1} = q^{n+1},\tag{14}$$

$$-\text{Ro }\Delta\psi^{n+1} + y = \overline{q}^{n+1},\tag{15}$$

where  $a^{n+1} = a(q^{n+1})$  and  $b^{n+1} = F^{n+1} + q^n/\Delta t$ .

In order to contain the computational cost, we opt for a segregated algorithm to solve coupled problem (13)-(15). A possible algorithm is as follows: given  $q^n$  and  $\psi^n$ , at  $t^{n+1}$  perform the following steps

(i) Find the vorticity  $q^{n+1}$  such that

$$\frac{1}{\Delta t}q^{n+1} + \nabla \cdot \left( \left( \nabla \times \psi^n \right) q^{n+1} \right) - \frac{1}{\text{Re}} \Delta q^{n+1} = b^{n+1}, \tag{16}$$

where we have replaced  $\psi^{n+1}$  in (13) by  $\psi^n$ , i.e. a linear extrapolation. (ii) Find the filtered vorticity  $\overline{q}^{n+1}$  such that

$$-\alpha^2 \nabla \cdot \left( a^{n+1} \nabla \overline{q}^{n+1} \right) + \overline{q}^{n+1} = q^{n+1}. \tag{17}$$

(iii) Find the stream function  $\psi^{n+1}$  such that

$$-\operatorname{Ro}\Delta\psi^{n+1} + y = \overline{q}^{n+1}.\tag{18}$$

For the space discretization of problem (16)–(18), we partition the computational domain  $\Omega$  into cells or control volumes  $\Omega_i$ , with  $i=1,\ldots,N_c$ , where  $N_c$  is the total number of cells in the mesh. We adopt a Finite Volume (FV) approximation that is derived directly from the integral form of the governing equations.

The integral form of Eq. (16) for each volume  $\Omega_i$  is given by:

$$\begin{split} &\frac{1}{\Delta t} \, \int_{\Omega_i} q^{n+1} d\Omega + \int_{\Omega_i} \nabla \cdot \left( \left( \nabla \times \psi^n \right) q^{n+1} \right) d\Omega \\ &- \frac{1}{Re} \int_{\Omega_i} \Delta q^{n+1} d\Omega = \int_{\Omega_i} b^{n+1} d\Omega \, . \end{split}$$

By applying the Gauss-divergence theorem, the above equation becomes:

$$\frac{1}{\Delta t} \int_{\Omega_i} q^{n+1} d\Omega + \int_{\partial \Omega_i} \left( \left( \nabla \times \psi^n \right) q^{n+1} \right) \cdot d\mathbf{A} 
- \frac{1}{Re} \int_{\partial \Omega_i} \nabla q^{n+1} \cdot d\mathbf{A} = \int_{\Omega_i} b^{n+1} d\Omega,$$
(19)

where **A** is the surface vector associated with the boundary of  $\Omega_i$ . Then, the discretized form of Eq. (19), divided by the control volume  $\Omega_i$ , can be written as:

$$\frac{1}{\Delta t} q_i^{n+1} + \sum_j \varphi_j^n q_{i,j}^{n+1} - \frac{1}{Re} \sum_j (\nabla q_i^{n+1})_j \cdot \mathbf{A}_j = b_i^{n+1}, \tag{20}$$

where  $\mathbf{A}_j$  is the surface vector of the jth face of the control volume and  $\varphi_j^n = (\nabla \times \psi_j^n) \cdot \mathbf{A}_j$ . In (20),  $q_i^{n+1}$  and  $b_i^{n+1}$  denote the average potential vorticity and discrete source term in control volume  $\Omega_i$ , while  $q_{i,j}^{n+1}$  represents the potential vorticity associated to the centroid of face j normalized by the volume of  $\Omega_i$ . For more details about on the treatment of the convective and diffusive terms, the reader is referred to [20,27]

We deal with the space approximations of Eq. (17) and (18) in an analogous way and obtain:

$$-\alpha^{2} \sum_{i} a_{j}^{n+1} \left( \nabla \bar{q}_{i}^{n+1} \right)_{j} \cdot \mathbf{A}_{j} + \bar{q}_{i}^{n+1} = q_{i}^{n+1}, \tag{21}$$

$$-Ro\sum_{i} \left(\nabla \psi_{i}^{n+1}\right)_{j} \cdot \mathbf{A}_{j} + y_{i} = \overline{q}_{i}^{n+1}, \tag{22}$$

respectively.

In summary, the fully discretized form of problem (9)–(11) is given by system (20)–(22). For the implementation of the numerical scheme described in this section, we chose the FV C++ library OpenFOAM [28].

# 3. Numerical results

This section presents several numerical results for the QGE (i.e., no turbulence model), BV- $\alpha$ , and BV-NL- $\alpha$  models. We consider a benchmark test that has been widely used to analyze new techniques for turbulence in geophysical flows: the double-gyre wind forcing experiment [13–16,21,29].

The computational domain is rectangle  $[0, 1] \times [-1, 1]$  and the forcing is prescribed by setting  $F = \sin(\pi y)$ . We consider two different cases:

- Case 1: Ro = 0.0036 and Re = 450;
- Case 2: Ro = 0.008 and Re = 1000.

The BV- $\alpha$  model has been successfully tested for Ro=0.0016 and Re=200 [13–16]. We chose Case 1 because it has been studied in [29] with an Approximate Deconvolution model discretized with a Finite Element (FE) method. However, to the best of our knowledge it is the first time that larger values of Ro and Re as in Case 2 are considered. Although the Munk scale (8) is the same for both cases ( $\delta_M/L=0.02$ ), we will show that Case 2 is more critical due to the larger Reynolds number. Since the Munk scale has the same dependence on Ro and Re, it is surprising that Case 2 (i.e., smaller Re) is more challenging than Case 1 (i.e., smaller Re). However, this is in line with what observed in [29]: the simulation of a flow with higher values of Re becomes unphysical with finer meshes than the simulation of a flow with lower values of Re and equal Munk scale.

In order to validate our approach, we proceed as follows. First, we perform a QGE simulation with the high resolution mesh 256  $\times$  512 [22,29], which has a mesh size (h=1/256) almost 20 times smaller than the Munk scale. Then, we run experiments on two coarse meshes,  $16 \times 32$  (h=1/16) and  $4 \times 8$  (h=1/4), with the QGE, BV- $\alpha$ , and BV-NL- $\alpha$  models and compare the results with the high resolution QGE solution. We run all the simulations from  $t_0=0$  to T=100, with time step  $\Delta t=2.5e-5$  [22] Since time discretization with BDF1 is known to introduce substantial numerical diffusion, for Case 1 we will compare the results obtained with both BDF1 and BDF2. For all the simulations performed with the BV- $\alpha$  and BV-NL- $\alpha$  models, we set  $\alpha=h$  following [14].

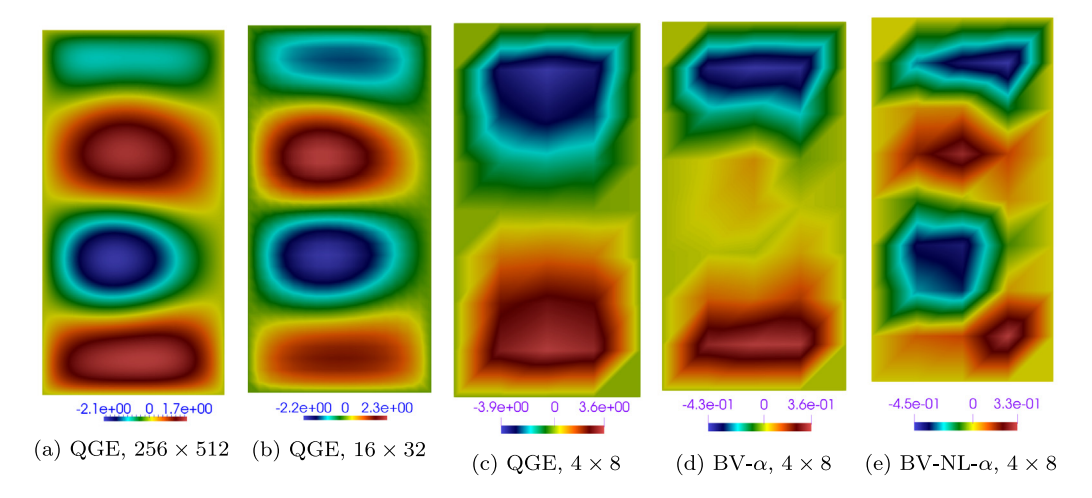


Fig. 1. Case 1:  $\widetilde{\psi}$  computed with different models, different meshes, and BDF1. The specific model and mesh for each panel is reported in the corresponding subcaption.

The quantities of interest for this benchmark are the time-averaged stream function  $\widetilde{\psi}$  and the time-averaged potential vorticity  $\widetilde{q}$  over time interval [20, 100], and the kinetic energy of the system E:

$$E = \frac{1}{2} \int_{\Omega} \left( \left( \frac{\partial \psi}{\partial y} \right)^2 + \left( \frac{\partial \psi}{\partial x} \right)^2 \right) d\Omega. \tag{23}$$

When we use the BV-NL- $\alpha$  model, we will also compute the time-averaged indicator function  $\tilde{a}$  over time interval [20, 100].

# 3.1. Case 1

In this section, we present the numerical results for Case 1. We report in Figs. 1(a) and 2 (a) the time-averaged stream function  $\widetilde{\psi}$  and potential vorticity  $\widetilde{q}$  computed with the QGE model, high resolution mesh 256  $\times$  512, and BDF1. The corresponding counterparts obtained with BDF2 are shown in Figs. 3(a) and 4 (a). First of all, we notice the stream functions computed with BDF1 and BDF2 show 4 gyres with the same shape. As expected though, the positive and negative peaks are smoothed out when using BDF1. We also observe very good agreement with the solution in [22,29], which was computed with a FE method. The time evolution of the kinetic energy E is reported with a black line in Fig. 5 for BDF1 and in Fig. 6 for BDF2. We observe that, while the phases given by BDF1 and BDF2 are not in agreement, the average kinetic energy and its amplitude agree well. Hereinafter, we will refer to the solution computed with the QGE model on mesh 256  $\times$  512 as the true solution.

In [29], it is shown that the time-averaged stream function given by the QGE model and computed by a FE method with the mesh  $16 \times 32$  (i.e., with a mesh size about 3 times bigger than the Munk scale) incorrectly exhibits just two gyres instead of the four gyres seen in Fig. 1(a). However, we observe that the QGE model approximated with our FV method works quite well even with mesh  $16 \times 32$ : with both BDF1 and BDF2 it captures the four-gyre pattern and the magnitude is mostly close to that of the true solution although some overshoots are seen. Compare Fig. 1(b) with Fig. 1(a) and Fig. 3(b) with Fig. 3(a). The time-averaged potential vorticity computed with mesh  $16 \times 32$  is also in good agreement with the true  $\tilde{q}$ : compare Fig. 2(b) with Fig. 2(a) and Fig. 4(b) with Fig. 4(a). For this quantity, the magnitudes are even closer and no overshoot is observed. A possible reason for the better performance of our FV method with respect to a FE method could be the following: it yields exact conservation and thus provides acceptable results despite using a mesh with a mesh size larger than the Munk scale.

We had to push the coarseness of the mesh to  $4 \times 8$  to see that the solution provided by the QGE model fails to show the four-gyre pattern. See Fig. 1(c) for BDF1 and Fig. 3(c) for BDF2. We see that the extra artificial diffusion introduced by the BDF1 scheme is not sufficient to recover the four-gyre structure with this coarse mesh. In addition, notice how the maximum and minimum values of  $\psi$  computed mesh  $4 \times 8$  are both larger (in absolute value) than the true values. Similarly, the  $\tilde{q}$  computed with mesh  $4 \times 8$  is not close to the true solution (see Fig. 2(c) for BDF1 and Fig. 4(c) for BDF2) and the kinetic energy is off (see Figs. 5 and 6, top panels). In particular, the kinetic energy computed with mesh  $4 \times 8$  reaches higher values for most of the time interval, regardless of whether one uses BDF1 or BDF2. These poor results are to be expected, since the size of mesh  $4 \times 8$  is over 12 times larger than the Munk scale. If we use the BV- $\alpha$  model to represent the unsolved scales with the same mesh, we observe a slight improvement in the time-averaged potential vorticity. See Fig. 2(d) for BDF1 and 4 (d) for BDF2. However, the time-averaged stream function still exhibits an incorrect

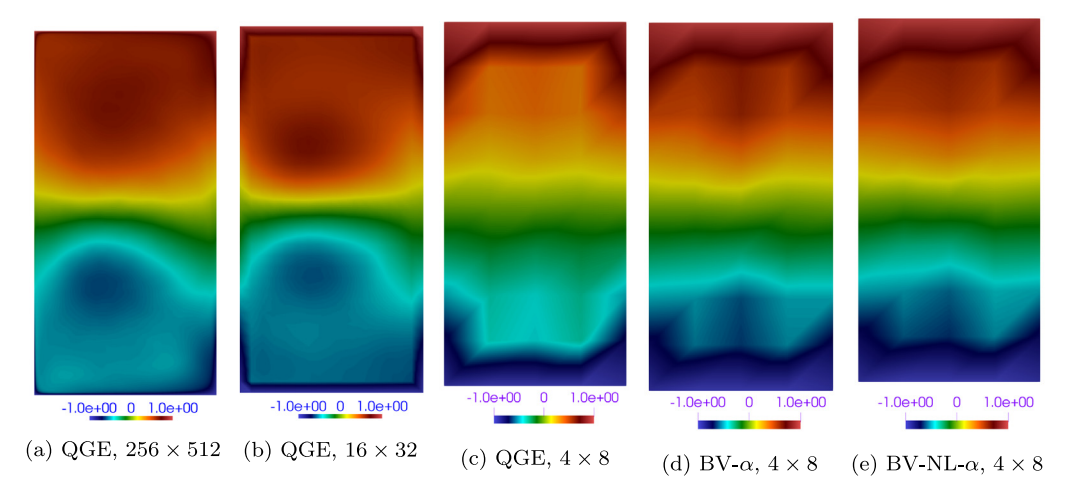


Fig. 2. Case 1:  $\widetilde{q}$  computed with different models, different meshes, and BDF1. The specific model and mesh for each panel is reported in the corresponding subcaption.

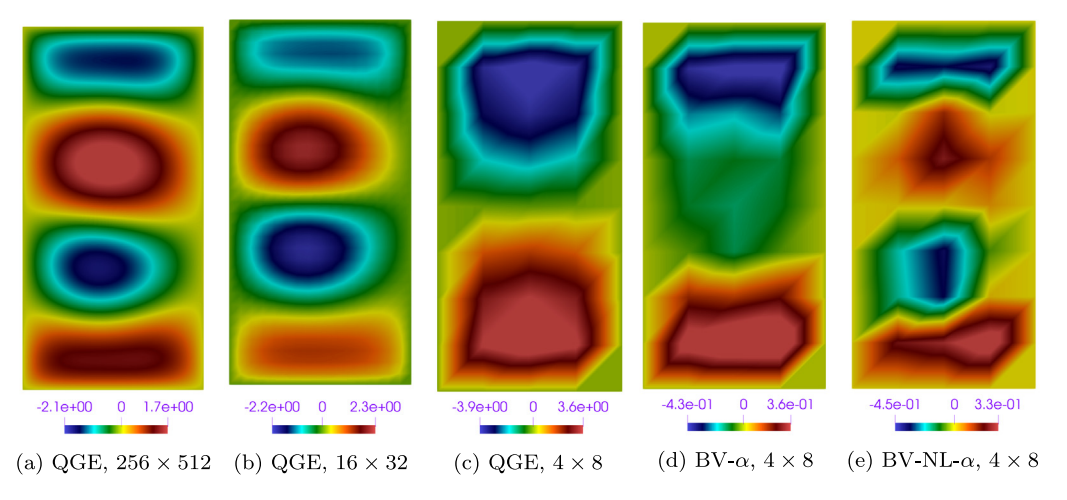


Fig. 3. Case 1:  $\widetilde{\psi}$  computed with different models, different meshes, and BDF2. The specific model and mesh for each panel is reported in the corresponding subcaption.

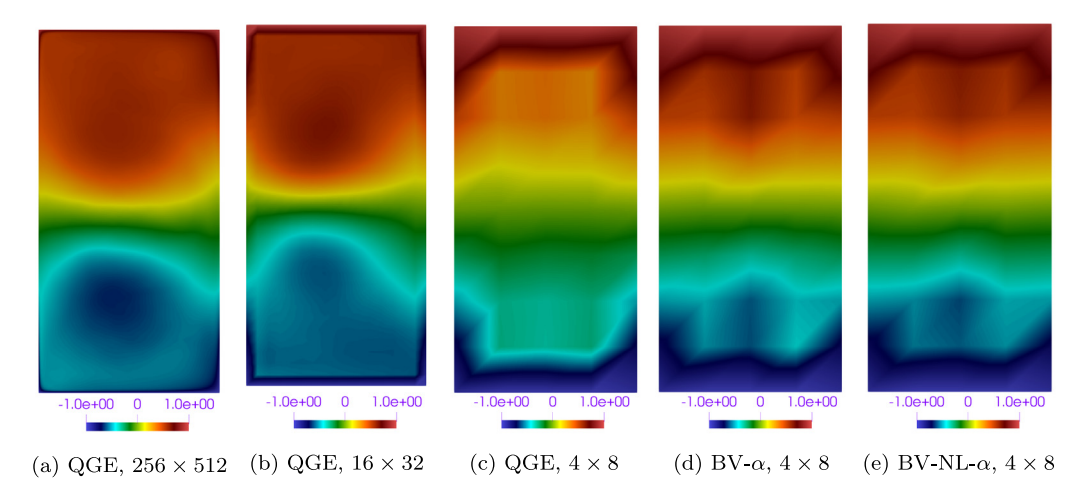
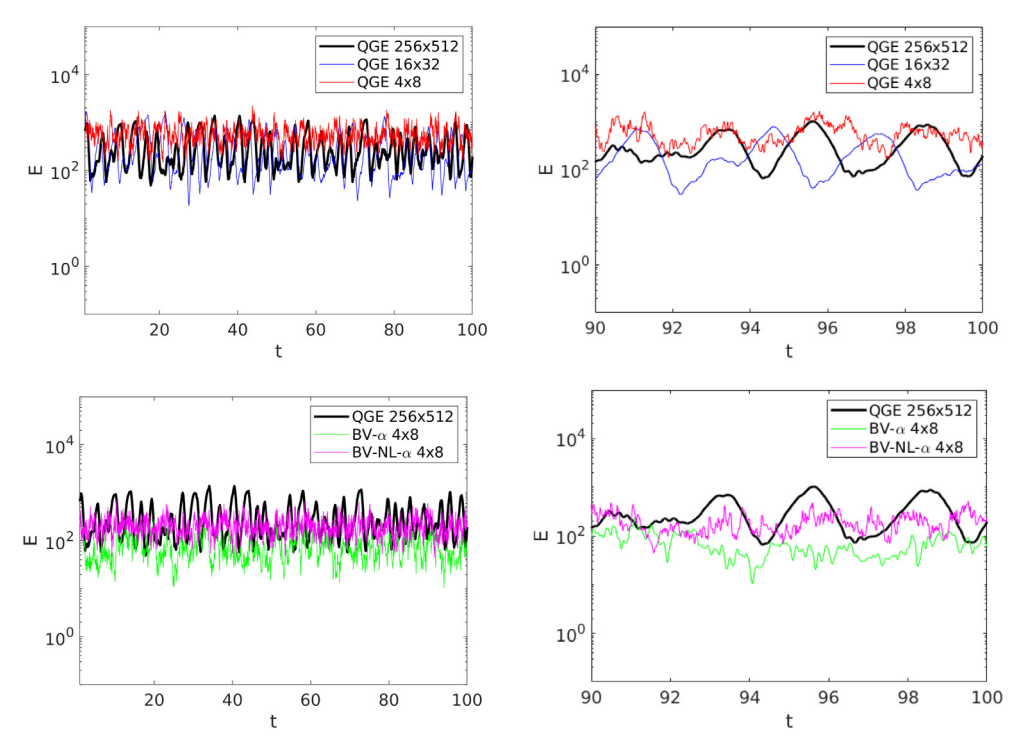
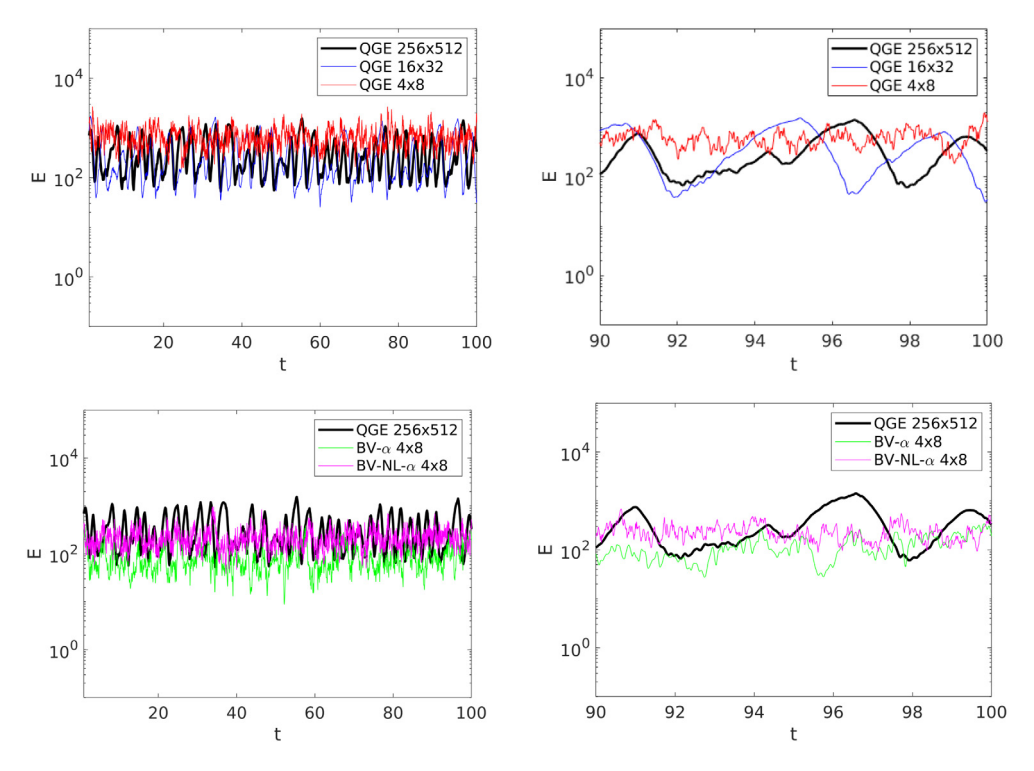


Fig. 4. Case 1:  $\widetilde{q}$  computed with different models, different meshes, and BDF2. The specific model and mesh for each panel is reported in the corresponding subcaption.



**Fig. 5.** Case 1: time evolution of the kinetic energy computed by the QGE model with all the meshes and BDF1 (top, left) and corresponding zoomed-in view (top, right); time evolution of the kinetic energy computed by the QGE model with the finest mesh, BV- $\alpha$  and BV-NL- $\alpha$  with the coarsest mesh and BDF1 (bottom, left) and corresponding zoomed-in view (bottom, right).



**Fig. 6.** Case 1: time evolution of the kinetic energy computed by the QGE model with all the meshes and BDF2 (top, left) and corresponding zoomed-in view (top, right); time evolution of the kinetic energy computed by the QGE model with the finest mesh, BV- $\alpha$  and BV-NL- $\alpha$  on the coarsest mesh and BDF2 (bottom, left) and corresponding zoomed-in view (bottom, right).

**Table 1** Case 1: Computational times required by the QGE, BV- $\alpha$  and BV-NL- $\alpha$  models with different meshes and BDF2.

Model	Mesh	CPU time [s]
QGE	256 × 512	187763
QGE	16 × 32	1453
QGE	4 × 8	871
BV-α	4 × 8	1620
BV-NL- $\alpha$	4 × 8	1653

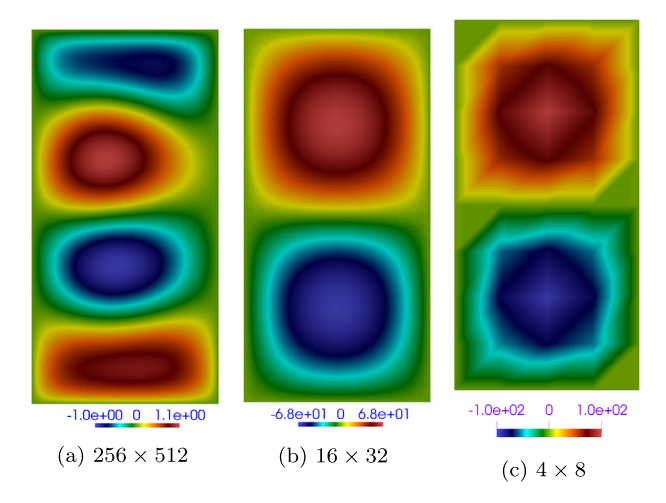


**Fig. 7.** Case 2:  $\widetilde{\psi}$  computed by the QGE model with different meshes.

pattern (a three-gyre structure instead of four gyres, with the third gyre more visible when using BDF1) and its magnitude is significantly underestimated as shown in Figs. 1(d) and 3 (d). In addition, the bottom panels of Figs. 5 and 6 show that the kinetic energy given by the BV- $\alpha$  model with both BDF1 and BDF2 is much smaller than the true kinetic energy over the entire time interval of interest and the frequency is off. The BV-NL- $\alpha$  model represents an improvement over the BV- $\alpha$  model since it is able to recover the four-gyre pattern of the time-averaged stream function (see Fig. 1(e) for BDF1 and Fig. 3(e) for BDF2) and it provides an average kinetic energy comparable with the true one (see Figs. 5 and 6, bottom panels). However, the magnitude of the time-averaged stream function is much smaller than it should be, as it is expected when using a filter with such a coarse mesh, and the time-averaged vorticity is indistinguishable from the one computed by the BV- $\alpha$  model.

We conclude by reporting in Table 1 the computational times required by the different models and meshes used in this section. The times refer to the BDF2 scheme and are very similar to the times required by BDF1, which are omitted. The computation of the true solution takes about 52 h. The cost of the QGE model drops considerably as the mesh is coarsened. The time needed to complete the simulations with the BV- $\alpha$  model and mesh 4  $\times$  8 is almost double the time required by the QGE model with the same mesh, indicating that the cost of the filtering step is roughly the same as the cost of the QGE model. Finally, we observe that the improvement introduced by the nonlinear filter comes with a negligible additional cost with respect to the linear filter.

# 3.2. Case 2

Let us now turn to Case 2. Since we did not observe major differences in the solutions obtained with BDF1 and BDF2 for Case 1, we will present only the results given by BDF1. Once again we start with the QGE model and mesh  $256 \times 512$ . Figs. 7(a) and 8(a) display the time-averaged stream function  $\widetilde{\psi}$  and potential vorticity  $\widetilde{q}$ , respectively. We will refer to this solution as the *true* solution. The corresponding kinetic energy E is shown in Fig. 9 with a black line.

For a simple comparison on the effects of increased Reynolds and Rossby numbers, we display in Fig. 10 average vorticity streamlines for Case 1 and 2. When going from Case 1 to Case 2, the region with higher average vorticity (dark red) expands and moves South-West, while the region with the smaller average vorticity (dark blue) moves North-East as it expands. In addition, we see differences on the Western boundary.

Next, we stick to the QGE model but consider coarser meshes. We notice that while in Case 1 the QGE model with mesh  $16 \times 32$  provided a physical solution, that is it no more true for Case 2. In fact, by comparing Fig. 7(b) with Fig. 7(a) we see that the time-averaged stream function computed with mesh  $16 \times 32$  exhibits an incorrect two-gyre pattern and a

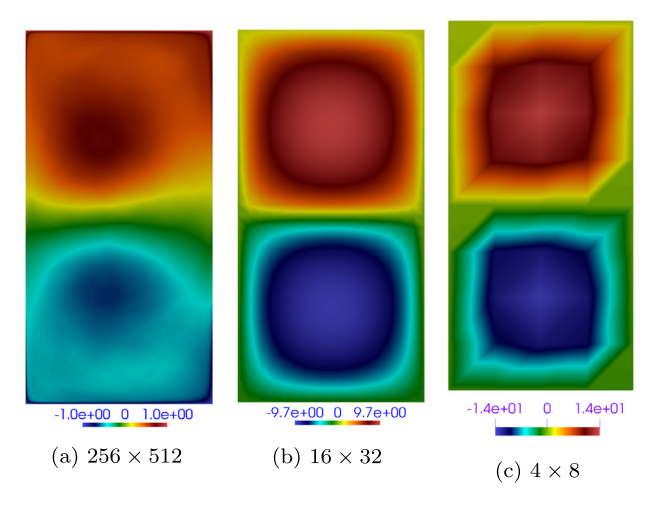


**Fig. 8.** Case 2:  $\widetilde{q}$  computed by the QGE model with different meshes.

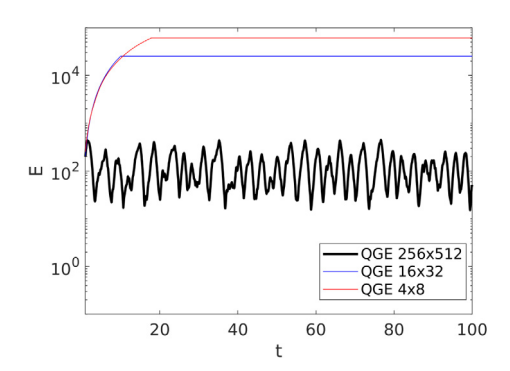


Fig. 9. Case 2: time evolution of the kinetic energy computed by the QGE model with different meshes.

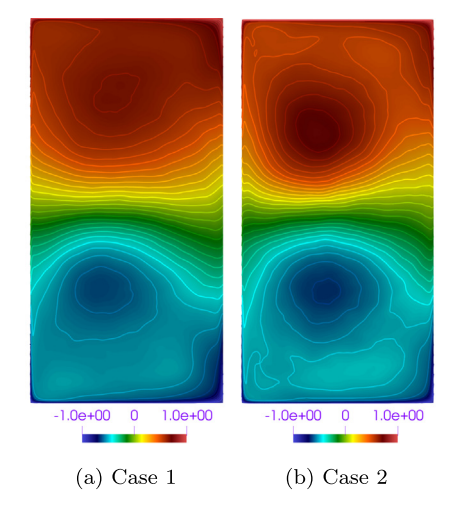
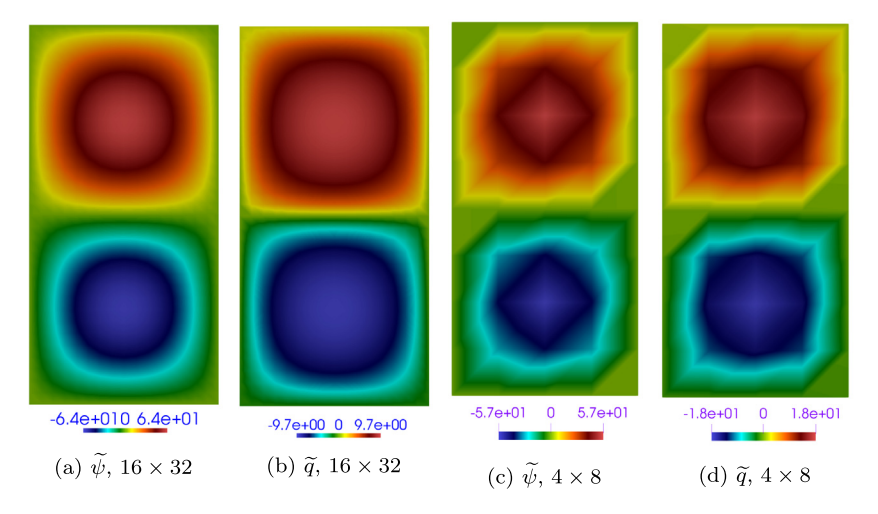


Fig. 10. Average vorticity streamlines computed with mesh 256  $\times$  512 and BDF1 for (a) Case 1 and (b) Case 2.

magnitude almost 70 times larger than the true solution. Similarly, the time-averaged potential vorticity shows a different pattern and a much larger magnitude. Compare Fig. 8(b) and (a). In addition, from Fig. 9 we see that the kinetic energy computed with mesh  $16 \times 32$  is not oscillatory and takes values much larger (up to about two orders of magnitude) than the true kinetic energy. Even poorer results are obtained with mesh  $4 \times 8$ . See Figs. 7(c), 8 (c), and 9.



**Fig. 11.** Case 2:  $\widetilde{\psi}$  and  $\widetilde{q}$  computed with the BV- $\alpha$  model and meshes 16  $\times$  32 and 4  $\times$  8.

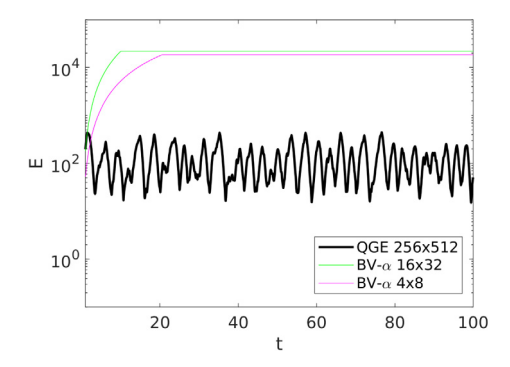


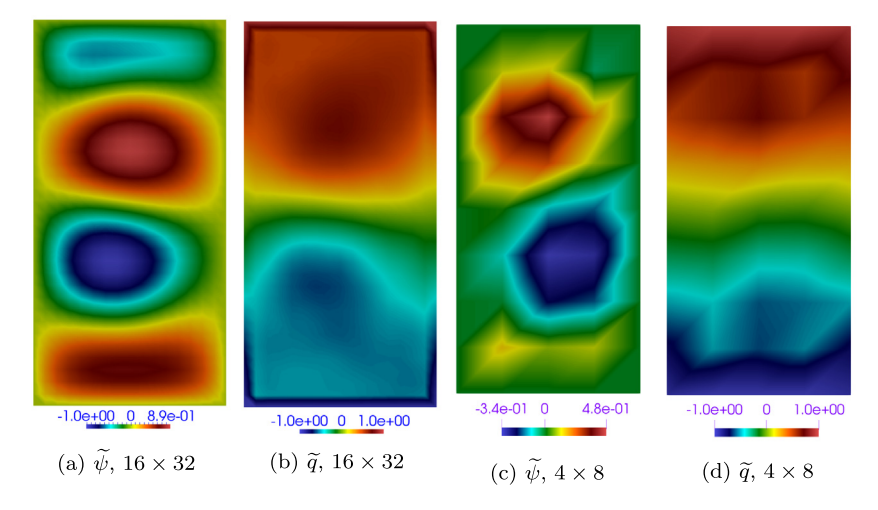
Fig. 12. Case 2: time evolution of the kinetic energy computed by the BV- $\alpha$  model with meshes 16  $\times$  32 and 4  $\times$  8 and compared to the true kinetic energy.

Fig. 11 shows  $\widetilde{\psi}$  and  $\widetilde{q}$  computed with the BV- $\alpha$  model and meshes 16  $\times$  32 and 4  $\times$  8. We observe no improvement over the QGE model with either mesh. This is confirmed by the computed kinetic energy reported in Fig. 12. The solution computed with the BV-NL- $\alpha$  model and mesh 16  $\times$  32 is shown in Fig. 13(a) and (b). It does represent a significant improvement: the computed  $\widetilde{\psi}$  and  $\widetilde{q}$  are in very good agreement with the exact solution both in terms of pattern and magnitude. The kinetic energy computed with the BV-NL- $\alpha$  model and mesh 16  $\times$  32 is also in good agreement with the exact kinetic energy. In fact, Fig. 14 shows that the amplitudes and frequencies of oscillation are comparable, although the phases are off. Even with the coarsest mesh under consideration (mesh 4  $\times$  8) the BV-NL- $\alpha$  model captures the solution pattern better than the QGE and BV- $\alpha$  models, although the magnitude of  $\widetilde{\psi}$  is reduced by the nonlinear filter. The average kinetic energy computed with the BV-NL- $\alpha$  model and mesh 4  $\times$  8 is also in good agreement with the true average kinetic energy. See Fig. 14.

Let us conclude with the visualization of the time-averaged indicator function  $\widetilde{a}$  computed with the meshes  $16 \times 32$  and  $4 \times 8$  shown in Fig. 15. We see that  $\widetilde{a}$  takes its the largest values in one strip of cells close to the boundary, where there are the largest gradients of the potential vorticity. In particular, in Fig. 15(a) we see that the action of the nonlinear filter is more important close to the Western boundary, i.e., on the left side  $\widetilde{a}$  takes larger values over a larger strip. This is less evident in Fig. 15(b) due to the extreme coarseness of the mesh. Notice also that the maximum and minimum values of  $\widetilde{a}$  become larger in absolute value when the mesh gets coarser, since more regularization is needed.

#### 4. Conclusions and perspectives

We presented a nonlinear variant of the BV- $\alpha$  model, called BV-NL- $\alpha$ , for the simulation of barotropic flows with under-refined meshes. To select the regions of the domain where filtering is needed, we employed a nonlinear differential low-pass filter. For the space discretization of the BV-NL- $\alpha$  model, we chose a Finite Volume method that has the advantage of enforcing conservation of quantities at the discrete level.



**Fig. 13.** Case 2:  $\widetilde{\psi}$  and  $\widetilde{q}$  computed with the BV-NL- $\alpha$  model and meshes 16  $\times$  32 and 4  $\times$  8.

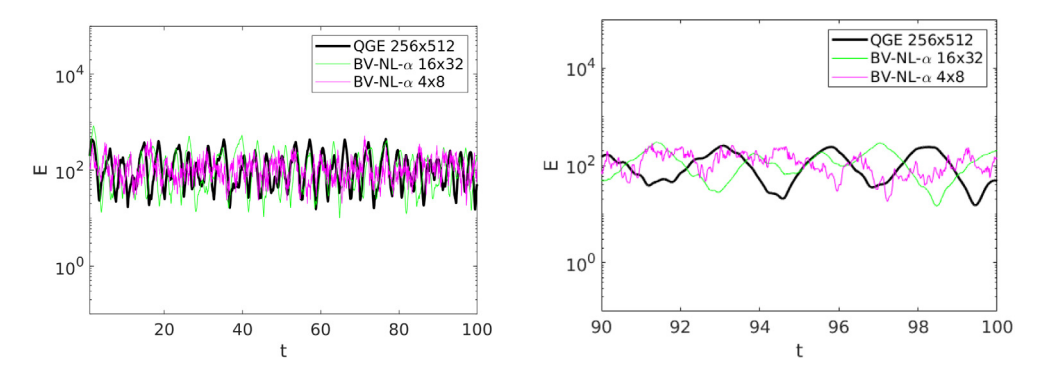


**Fig. 14.** Case 2: time evolution of the kinetic energy computed by the BV-NL- $\alpha$  model with meshes 16  $\times$  32 and 4  $\times$  8 and compared to the true kinetic energy (left) and corresponding zoomed-in view (right).

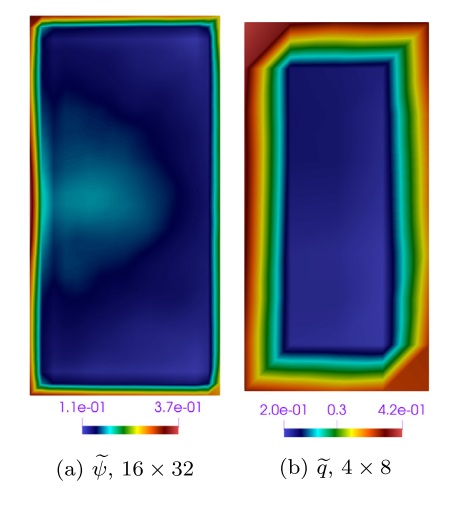


**Fig. 15.** Case 2:  $\widetilde{a}$  computed with the BV-NL- $\alpha$  model and meshes 16  $\times$  32 and 4  $\times$  8.

We showed the effectiveness of our approach through a computational study for the double-gyre wind forcing benchmark. We considered two different parameters setting: (i) Ro = 0.0036 and Re = 450 and (ii) Ro = 0.008 and

Re=1000. In both cases, when coarse meshes are considered the BV-NL- $\alpha$  model provides more accurate results than the OGE and BV- $\alpha$  models.

This work could be expanded in different directions. A sensitivity analysis for the filtering radius [30] would help us understand how to obtain the most accurate results when compared to a direct numerical simulation. Moreover, it would be interesting to test the performance of a class of deconvolution-based indicator functions and to implement an efficient algorithm called Evolve-Filter-Relax, which proved to work well for the Leray- $\alpha$  model [19,20,31–35]. Thus, we believe they could be successful also for the BV-NL- $\alpha$  model.

#### Data availability

Data will be made available on request.

## Acknowledgments

We acknowledge the support provided by the European Research Council Executive Agency by the Consolidator Grant project AROMA-CFD "Advanced Reduced Order Methods with Applications in Computational Fluid Dynamics" - GA 681447, H2020-ERC CoG 2015 AROMA-CFD, PI G. Rozza, and INdAM-GNCS 2019–2020 projects. This work was also partially supported by US National Science Foundation through grant DMS-1953535. A. Quaini also acknowledges support from the Radcliffe Institute for Advanced Study at Harvard University where she has been the 2021–2022 William and Flora Hewlett Foundation Fellow.

#### References

- [1] A. Kolmogorov, The local structure of turbulence in incompressible viscous fluids at very large Reynolds numbers, Dokl. Akad. Nauk SSSR 30 (1941) 301–305.
- [2] A. Kolmogorov, Dissipation of energy in isotropic turbulence, Dokl. Akad. Nauk SSSR 32 (1941) 19-21.
- [3] R. Kraichnan, Inertial ranges in two-dimensional turbulence, Phys. Fluids 10 (1967) 1417.
- [4] G. Batchelor, Computation of the energy spectrum in homogeneous two-dimensional turbulence, Phys. Fluids 12 (1969) 233.
- [5] C. Leith, Atmospheric predictability and two-dimensional turbulence, J. Atmos. Sci. 28 (1971) 145-161.
- [6] G. Vallis, Atmospheric and Oceanic Fluid Dynamics, Cambridge University Press, 2006.
- [7] B. Cushman-Roisin, J. Beckers, Introduction to Geophysical Fluid Dynamics: Physical and Numerical Aspects, Academic Press, 2011.
- [8] J. McWilliams, Fundamentals of Geophysical Fluid Dynamics, Cambridge University Press, 2006.
- [9] O. San, A. Staples, T. Iliescu, Approximate deconvolution large eddy simulation of a stratified two-layer quasigeostrophic ocean model, Ocean Model. 63 (2012) 1–20.
- [10] G. Carere, M. Strazzullo, F. Ballarin, G. Rozza, R. Stevenson, A weighted POD-reduction approach for parametrized PDE-constrained optimal control problems with random inputs and applications to environmental sciences, Comput. Math. Appl. 102 (2021) 261–276.
- [11] M. Strazzullo, F. Ballarin, R. Mosetti, G. Rozza, Model reduction for parametrized optimal control problems in environmental marine sciences and engineering, SIAM J. Sci. Comput. 40 (2017) B1055–B1079.
- [12] C. Mou, Z. Wang, D. Wells, X. Xie, T. Iliescu, Reduced order models for the quasi-geostrophic equations: A brief survey, Fluids 6 (2020) 16.
- [13] B. Nadiga, L. Margolin, Dispersive-dissipative eddy parameterization in a barotropic model, J. Phys. Oceanogr. 31 (2001) 2525-2531.
- [14] D. Holm, B. Nadiga, Modeling mesoscale turbulence in the barotropic double-gyre circulation, J. Phys. Oceanogr. 33 (2003) 2355–2365.
- [15] I. Monteiro, C. Manica, L. Rebholz, Numerical study of a regularized barotropic vorticity model of geophysical flow, Numer. Methods Partial Differential Equations 31 (2015) 1492–1514.
- [16] I. Monteiro, C. Carolina, Improving numerical accuracy in a regularized barotropic vorticity model of geophysical flow, Int. J. Numer. Anal. Modell. Ser. B 5 (2014) 317–338.
- [17] W. Layton, L. Rebholz, C. Trenchea, Modular nonlinear filter stabilization of methods for higher Reynolds numbers flow, J. Math. Fluid Mech. 14 (2012) 325–354.
- [18] A. Bowers, L. Rebholz, Numerical study of a regularization model for incompressible flow with deconvolution-based adaptive nonlinear filtering, Comput. Methods Appl. Mech. Engrg. 258 (2013) 1–12.
- [19] L. Bertagna, A. Quaini, A. Veneziani, Deconvolution-based nonlinear filtering for incompressible flows at moderately large Reynolds numbers, Internat. J. Numer. Methods Fluids 81 (8) (2016) 463–488.
- [20] M. Girfoglio, A. Quaini, G. Rozza, A finite volume approximation of the Navier-Stokes equations with nonlinear filtering stabilization, Comput. & Fluids 187 (2019) 27–45.
- [21] R. Greatbatch, B. Nadiga, Four-gyre circulation in a barotropic model with double-gyre wind forcing, J. Phys. Oceanogr. 30 (2000) 1461-1471.
- [22] O. San, T. Iliescu, A stabilized proper orthogonal decomposition reduced-order model for large scale quasigeostrophic ocean circulation, Adv. Comput. Math. 41 (2014) 1289–1319.
- [23] J. Borggaard, T. Iliescu, J. Roop, A bounded artificial viscosity large eddy simulation model, SIAM J. Numer, Anal. 47 (2009) 622-645.
- [24] J. Hunt, A. Wray, P. Moin, Eddies Stream and Convergence Zones in Turbulent Flows, Tech. Rep. CTR-S88, CTR report, 1988.
- [25] A. Vreman, An eddy-viscosity subgrid-scale model for turbulent shear flow: Algebraic theory and applications, Phys. Fluids 16 (2004) 3670.
- [26] A.L. Bowers, L.G. Rebholz, A. Takhirov, C. Trenchea, Improved accuracy in regularization models of incompressible flow via adaptive nonlinear filtering, Internat. J. Numer. Methods Fluids 70 (2012) 805–828.
- [27] M. Girfoglio, A. Quaini, G. Rozza, A POD-Galerkin reduced order model for the Navier-Stokes equations in stream function-vorticity formulation, Comput. & Fluids 244 (2022) 105536.
- [28] H.G. Weller, G. Tabor, H. Jasak, C. Fureby, A tensorial approach to computational continuum mechanics using object-oriented techniques, Comput. Phys. 12 (1998) 620–631.
- [29] O. San, A. Staples, Z. Wang, T. Iliescu, Approximate deconvolution large eddy simulation of a barotropic ocean circulation model, Ocean Model. 40 (2011) 120–132.
- [30] L. Bertagna, A. Quaini, L. Rebholz, A. Veneziani, On the sensitivity to the filtering radius in Leray models of incompressible flow, in: Contributions to Partial Differential Equations and Applications. Computational Methods in Applied Sciences, vol 47, Springer, Cham, 2019, pp. 111–130.

- [31] M. Girfoglio, A. Quaini, G. Rozza, Fluid-structure interaction simulations with a LES filtering approach in solids4Foam, Commun. Appl. Ind. Math. 12 (2021) 13–28.
- [32] M. Girfoglio, A. Quaini, G. Rozza, Pressure stabilization strategies for a LES filtering reduced order model, Fluids 6 (2021) 302.
- [33] M. Girfoglio, A. Quaini, G. Rozza, A hybrid reduced order model for nonlinear LES filtering, 2021, https://arxiv.org/abs/2107.12933.
- [34] M. Girfoglio, A. Quaini, G. Rozza, A POD-Galerkin reduced order model for a LES filtering approach, J. Comput. Phys. 436 (2021) 110260.
- [35] M. Strazzullo, M. Girfoglio, F. Ballarin, T. Iliescu, G. Rozza, Consistency of the full and reduced order models for evolve-filter-relax regularization of convection-dominated, marginally-resolved flows, Int. J. Numer. Methods Eng 123 (14) (2022) 3148–3178.